CHALMERS
UNIVERSITY OF TECHNOLOGY

Fast, unconditional reset and leakage reduction in fixed-frequency transmon qubits

Downloaded from: https://research.chalmers.se, 2026-10-07 03:12 UTC

Citation for the original published paper (version of record):
Chen, L., Pettersson Fors, S., Yan, Z. et al (2026). Fast, unconditional reset and leakage reduction in fixed-frequency transmon qubits. npj Quantum Information, 12(1).
http://dx.doi.org/10.1038/s41534-026-01356-2

N.B. When citing this work, cite the original published paper.

research.chalmers.se offers the possibility of retrieving research publications produced at Chalmers University of Technology. It covers all kind of research output: articles, dissertations, conference papers, reports etc. since 2004. research.chalmers.se is administrated and maintained by Chalmers Library

(article starts on next page)

npj | quantum information

Article

Published in partnership with The University of New South Wales

https://doi.org/10.1038/s41534-026-01356-2

Fast, unconditional reset and leakage reduction in fixed-frequency transmon qubits

Check for updates

Liangyu Chen[1] ✉, Simon Pettersson Fors[1], Zixian Yan[1], Anaida Ali[1], Tahereh Abad[1], Tangyou Huang[1], Amr Osman[1], Eleftherios Moschandreou[1], Benjamin Lienhard[2,3], Sandoko Kosen[1], Hang-Xi Li[1], Daryoush Shiri[1], Tong Liu[1], Stefan Hill[1], Abdullah-Al Amin[1], Robert Rehammar[1], Mamta Dahiya[1], Andreas Nylander[1], Marcus Rommel[1], Anita Fadavi Roudsari[1], Marco Caputo[4], Leif Grönberg[4], Joonas Govenius[4], Miroslav Dobsicek[1], Michele Faucci Giannelli[1], Anton Frisk Kockum[1], Jonas Bylander[1] ✉ & Giovanna Tancredi[1] ✉

On-demand qubit-state initialization is a prerequisite for quantum computation. We demonstrate such a protocol in a device consisting of fixed-frequency transmon qubits pair-wise coupled via tunable couplers — an architecture that is also compatible with the surface code. We use tunable couplers to transfer any undesired qubit excitation to the readout resonator of the qubit, from which this excitation decays into the feedline. In total, the combination of multi-level qubit reset, leakage reduction, and coupler reset takes only 88 ns to complete. Our reset scheme is fast, unconditional, and achieves fidelities above 99%, thus enabling fixed-frequency qubit architectures as future implementations of fault-tolerant quantum computers.

The capability to reset a qubit to a known state on demand is an essential operation for quantum computation[1]. Qubit reset is becoming increasingly crucial for speeding up quantum algorithms and calibration, since lifetimes for superconducting qubits have extended to hundreds of microseconds and more[2–4], such that resetting by simply waiting for the qubit excitation to naturally decay becomes slow[5,6].

Protocols for qubit reset (that do not just wait for the qubit to decay) can be either conditional or unconditional, depending on whether or not they require knowledge of the qubit state. In conditional reset, the reset operation is conditioned on a previously measured result[7]: if the qubit is found in the first excited state $|1\rangle$, a π-pulse is applied to drive it back to its ground state $|0\rangle$. The primary limitation for conditional reset is the feedback time of the control electronics, and the success rate of the feedback operation depends on the readout fidelity. In unconditional reset, the excited state of the qubit is depopulated regardless of the initial qubit state[5,6,8–12]. Existing unconditional reset schemes typically require multiple drive signals, flux-tunable qubits, or additional control elements on the device. This added complexity makes it challenging to scale these schemes to a larger number of qubits.

Reset abilities that extend to higher qubit levels are required in quantum error correction (QEC) algorithms, crucial to achieve fault-tolerant quantum computing[13–15]. These QEC algorithms, e.g., the surface code that has been implemented in superconducting qubits, rely on repeated parity measurements[16–20]. In these codes, the physical qubits are designated as either data or ancilla qubits, distributed in a checkerboard pattern. The data qubits are parity-checked by measuring the ancilla qubits in each error-correction cycle. Each parity check is followed by a reset of the ancilla qubits to prepare them for the next round of error detection. However, during the cycle, data and ancilla qubits are prone to leakage outside of their computational subspace due to imperfections in the single- and two-qubit gates, measurement-induced transitions, and high-energy radiation impact, fatally compromising the QEC algorithms[8,11,21–24]. Therefore, fast, high-fidelity, multi-level reset for ancilla qubits and a leakage-reduction unit (LRU) for data qubits are both instrumental for practical QEC.

Implementing an LRU requires resetting only the $|2\rangle$ state or higher-energy states without disturbing the computational subspace, which consists of the $|0\rangle$ and $|1\rangle$ states. An LRU can be implemented either by directly coupling the $|2\rangle$-state population to a lossy resonator[21,23,25] or by performing a SWAP gate to transfer the $|2\rangle$-state population to another element on the processor[11,22]. It is crucial to develop an LRU that complements the reset strategy with the same architecture.

[1]Department of Microtechnology and Nanoscience, Chalmers University of Technology, Gothenburg, Sweden. [2]Department of Chemistry, Princeton University, Princeton, NJ, USA. [3]Department of Electrical and Computer Engineering, Princeton University, Princeton, NJ, USA. [4]VTT Technical Research Centre of Finland, Espoo, Finland. ✉e-mail: liangyuc@chalmers.se; jonas.bylander@chalmers.se; tancredi@chalmers.se

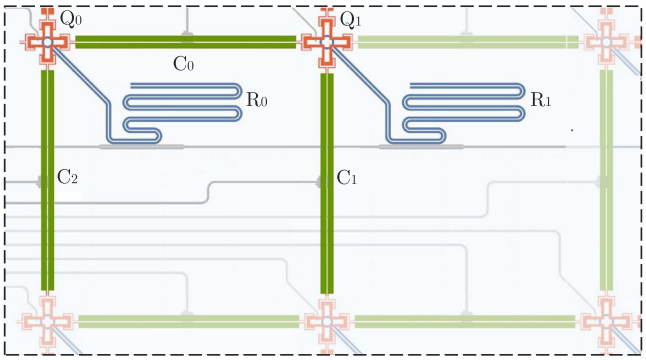

Fig. 1 | Subset of the 25-qubit device under test. The device has a flip-chip architecture[29], with the fixed-frequency qubits (red) and frequency-tunable couplers (green) placed on the qubit chip and the resonators (blue) and signal lines (gray) on the control chip interposer. A pair of qubits, Q_0 and Q_1, with their respective readout resonators, R_0 and R_1, and three of their couplers, C_0, C_1, and C_2, are involved in the experiments. Couplers C_0 and C_2 are used to reset qubit Q_0, and coupler C_1 is used to implement the leakage reduction unit on qubit Q_1.

In this article, we demonstrate both high-fidelity unconditional qubit reset and leakage reduction in an architecture consisting of superconducting fixed-frequency transmon qubits[26] pair-wise coupled via tunable couplers[27–29], as shown in Fig. 1. We propose a reset and leakage reduction scheme that uses the tunable coupler as a means to transfer excitations from a qubit to its readout resonator, from which the excitations can then decay into the feedline. We achieve five objectives with our schemes, summarized in Fig. 2:

1. A fast, adiabatic $|1\rangle$- to $|0\rangle$-state reset with an error of $(1.87 \pm 1.12) \times 10^{-3}$ within 9 ns.
2. An adiabatic reset that can simultaneously move both the $|1\rangle$- and $|2\rangle$-state populations to the $|0\rangle$ state, reaching an error of $(7.87 \pm 1.94) \times 10^{-3}$ within 61 ns.
3. An LRU that removes the $|2\rangle$-state population back to the $|1\rangle$ state without disrupting the computational subspace of the target qubit, with an error of 9.50×10^{-3} in 5 ns.
4. A coupler reset unit that dissipates the excitation through the qubit readout resonator within 27 ns.
5. Simultaneous reset of qubit Q_0 and leakage reduction of qubit Q_1 in a total time of 88 ns.

All operations are easy to implement with the current fixed-frequency qubits and tunable-coupler architecture without the need for any additional hardware resources. The total duration of 88 ns refers only to the applied reset and LRU sequence and does not include any extra dead time required after the operations for residual photons in the readout resonator to decay, which depends on the resonator linewidth and readout circuit design.

The experimental demonstration is carried out in a two-qubit subset of a 25-qubit device, which is illustrated in Fig. 1. More details on the device, fabrication, and performance are provided in the refs. 29,30. The qubits are designed to have frequencies within two frequency groups in a checkerboard pattern, with neighboring qubits separated in frequency by roughly 600 MHz[31]. The subset consists of two fixed-frequency transmon qubits Q_0 and Q_1[26] with transition frequencies $\omega_{Q_i}/2\pi$ at 5.176 and 4.534 GHz, and anharmonicities $\alpha_{Q_i}/2\pi$ at -256 and -158 MHz for $i = 0$ and 1, respectively. Each qubit is coupled with a strength $g_{qr} \approx 50$ MHz to a readout resonator R_i of frequency $\omega_{R_i}/2\pi = 6.752$ and 6.308 GHz for $i = 0$ and 1, respectively. Both resonators are coupled to the same feedline. There is a tunable coupler between each pair of qubits arranged in a square grid on the chip. In this experiment, three of the couplers (C_0, C_1, and C_2) surrounding the pair of qubits are used. The couplers are implemented as flux-tunable symmetric SQUID loops with maximal frequency $\omega_c/2\pi = 7.5$ GHz and anharmonicity $\alpha_c/2\pi = -80$ MHz. The qubit-to-coupler coupling rates $g_{qc}/2\pi$ are 40 MHz (60 MHz) for qubit Q_0 (Q_1). The coupling between the coupler and resonator has two main sources: a direct capacitive coupling due to their proximity on the chip and an indirect coupling mediated by the qubit. The device is cooled down to 10 mK and a microwave setup is used to measure the signal transmitted through the feedline. The complete experimental setup and device parameters resulting from basic characterization are reported in Suppl. Note I.

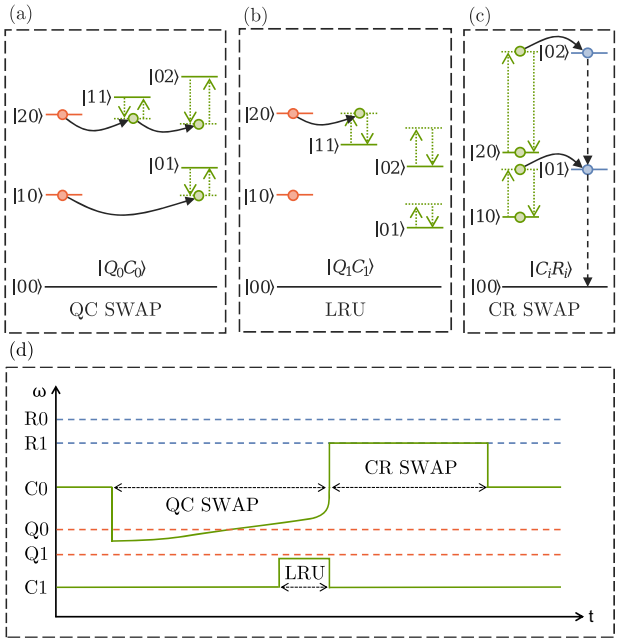

Operation	QC SWAP		LRU
Reset State	$\|1\rangle$	$\|1\rangle$ and $\|2\rangle$	$\|2\rangle$
Pulse Shape	Adiabatic	Adiabatic	Diabatic
Duration	9 ns	61 ns	5 ns
Error	1.87×10^{-3}	7.87×10^{-3}	9.50×10^{-3}

Fig. 2 | Schematic of the reset and leakage-reduction protocol. a In the reset protocol, the coupler C_0 is first tuned below and then adiabatically transits through Q_0 to implement a qubit-coupler (QC) SWAP gate. Q_1 is not affected due to the relatively large detuning between the two qubits. Note that the indicated transitions (black arrows) are a sketch of the more involved actual dynamics. **b** The coupler C_1 is used for the LRU, initially biased below the Q_1 frequency. **c** Afterwards, the coupler C_0 is tuned to higher frequencies to interact with the resonators to implement the coupler-resonator (CR) SWAP gate. The excitation will then decay into the environment via the readout feedline. **d** The full scheme, showing how the coupler frequencies (green) are tuned as a function of time with respect to the qubit (red) and resonator (blue) frequencies. The results for each type of operation are summarized in the inserted table.

The energy levels of the two-qubit subsystem are sketched in Fig. 2b–d. We aim to reset the high-frequency qubit, Q_0, and remove leakage on the low-frequency qubit, Q_1. To implement the reset protocol, the first step consists of a qubit-coupler (QC) SWAP gate where the excitation is moved from qubit Q_0 to coupler C_0. C_0 is parked above Q_0 to avoid any interaction with Q_1. Using a similar mechanism, the LRU is implemented on qubit Q_1 via coupler C_1, parked below Q_1. The QC SWAP and the LRU can be executed simultaneously on the respective qubit. Afterwards, the last step of the protocol involves the coupler-resonator (CR) SWAP gates for all couplers in parallel. The resonator excitation can then be dissipated through the feedline. These SWAP gates are implemented by tuning the coupler's frequency via the application of a magnetic flux pulse to its flux control line.

RESULTS

Qubit reset with adiabatic pulses

For qubit reset, one main scenario to consider is the ability to reset not just the qubit $|1\rangle$-state population, but also that of the higher energy states, due

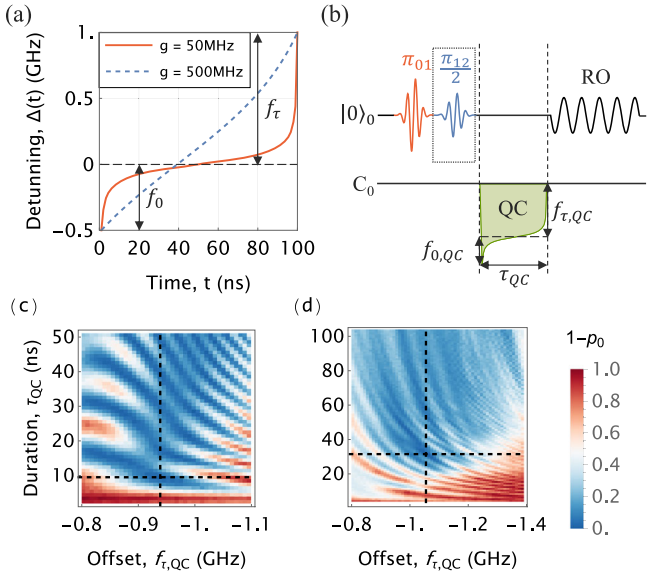

Fig. 3 | Calibration sequences of the reset protocols with adiabatic pulses. **a** Coupler detuning as a result of the adiabatic pulse for the qubit-coupler (QC) reset SWAP. The pulse is defined by four parameters: the pulse duration, $\tau = 100$ ns, the coupler frequency offset from Q_0, $f_\tau = 1$ GHz, an effective QC coupling strength, g, that sets the slope, and the QC detuning that defines the start of the adiabatic process, $f_0 = -0.5$ GHz. In particular, f_τ is essentially the amplitude of the flux pulse. Before the pulse starts, the coupler is at its idle frequency above Q_0, and the first point of the pulse diabatically shifts its frequency to be below Q_0, and then crosses the Q_0 energy level adiabatically before returning to the idle position. The given numerical values are for the specific example in (**a**). **b** The pulse schemes to calibrate the qubit-coupler (QC) SWAP include π_{01} (red) and $\pi_{12}/2$ (blue) pulses to prepare the qubit state, the flux pulses (filled areas in green) applied on the coupler, and the readout (RO) pulses on the resonator (black). **c**, **d** Measurement results of the qubit-coupler (QC) SWAP with the qubit initialized in (**c**) the $|1\rangle$ state and in (**d**) the superposition state $(|1\rangle + |2\rangle)/\sqrt{2}$. The color represents the reset error, which takes all non-ground state populations into account, and the regions with lower reset errors are always indicated in blue.

to the accumulation of leakage population outside of the computational subspace. For this reason, an adiabatic pulse is chosen to perform qubit reset due to the possibility of transferring the population from multiple energy levels simultaneously. The pulse shape is calculated from the instantaneous approximate adiabatic condition. Given a Hamiltonian $H(t)$, for any two adjacent eigenstates $|\Psi_n(t)\rangle$ and $|\Psi_m(t)\rangle$ with corresponding eigenvalues $E_n(t)$ and $E_m(t)$, the evolution with duration τ is approximately adiabatic if the following condition is met ($\hbar = 1$ throughout this article):

$$\max_{0\le t\le\tau} \frac{|\langle\Psi_n(t)|\frac{\partial H(t)}{\partial t}|\Psi_m(t)\rangle|}{|E_n(t)-E_m(t)|^2} \ll 1. \quad (1)$$

This condition implies that the changes in the interactions between the states $|\Psi_n(t)\rangle$ and $|\Psi_m(t)\rangle$ at time t must be significantly smaller than the energy distance between the states. Note that this is a global condition and can be modified to an instantaneous condition. The instantaneous approximate adiabatic condition was previously used to accelerate Grover's algorithm in adiabatic quantum computation by Roland and Cerf[32,33], which has been studied and experimentally verified in two-level systems[34,35].

The exact analytical solution, derived in the subsection "Adiabatic pulse shaping" in the Methods section, allows us to know how the coupler frequency should change over time. In experiments, this information is translated into a flux-biasing pulse which produces the desired frequency change. An example of such a pulse, translated into coupler detuning, is shown and annotated in Fig. 3a. The pulse can be defined by four parameters: τ is the pulse duration, f_0 is the coupler frequency offset from the coupler idle point, f_τ is the qubit-coupler detuning at the end of the pulse, and g is a coupling parameter that defines the slope of the center region. In practice, g is initially set to be the same as the qubit-coupler coupling strength, g_{qc}, but is then treated as an adjustable variable to be optimized for better reset performance. With increasing g, the pulse gradually transforms from a square pulse with an extra tail to a linear ramp pulse, so that we have the full range to tune the adiabaticity of the transition induced by this pulse.

Qubit-coupler SWAP gate

The first step of our reset protocol is to transfer the $|1\rangle$-state population of qubit Q_0 to coupler C_0, as shown in Fig. 2a. We first bias the coupler C_0 to be at least 1 GHz above Q_0 and below its resonator R_0, which would be the common idling point chosen for implementing a parametric two-qubit gate. We prepare Q_0 in $|1\rangle$ (without the $\pi_{12}/2$ pulse, which performs half a swap of the populations in the $|1\rangle$ and $|2\rangle$ states) and then implement a QC SWAP operation between Q_0 and C_0 by applying the adiabatic flux pulse given by the solution of (1) [see (12) in Methods]. The pulse induces a population transfer between qubit and coupler, which is ideally adiabatic.

To tune up the QC SWAP gate, we need to acquire the pulse parameters in two separate 2D sweeps, since four parameters are needed to define the pulse. For each sweep, we define the reset error ϵ_{reset} to be the residual non-ground-state population after the operation, $1 - p_0$, where p_0 is the measured $|0\rangle$-state population of Q_0. We use the reset error as the figure of merit for the calibration.

We first measure the reset error as a function of the pulse duration τ_{QC} and the coupler frequency detuning $f_{\tau,QC}$. We set $f_{0,QC}$ and g to be 200 MHz and 71 MHz, respectively, given preliminary qubit and coupler spectroscopy results. The reset error as a function of τ_{QC} and $f_{\tau,QC}$ is shown in Fig. 3c, and a chevron pattern illustrating population transfer from the qubit to the coupler $|1\rangle$ state is observed. We then fix τ_{QC} and $f_{\tau,QC}$ to be the values that produce the lowest reset error, and sweep both g and $f_{0,QC}$ to refine the pulse shape, as shown in Fig. 3b. A large parameter space, with g being below 50 MHz and $f_{0,QC}$ being around -200 MHz, can be identified where the reset error approaches the readout limit. These initial results suggest that the fidelity of this swap operation can be above 99 %, limited by drifting qubit parameters and coupler flux bias currents. We achieve depopulation of the $|1\rangle$ state with a 9 ns QC SWAP gate between the target qubit Q_0 and the coupler. The other qubit in the pair, Q_1, is only negligibly affected by the flux pulse, since it is 642 MHz lower in frequency than Q_0. Therefore, the reset of the Q_0 can be performed independently of the state of Q_1; more details can be found in Suppl. Note II.

To show how we can reset both the $|1\rangle$-state and $|2\rangle$-state population of the target qubit simultaneously, we prepare Q_0 in a superposition state $(|1\rangle + |2\rangle)/\sqrt{2}$ with an additional $\pi_{12}/2$ pulse [see Fig. 3b] so that the effect on both states is visible with a single measurement. The coupler interacts with multiple qubit levels during the frequency tuning; see Fig. 7 in the Methods section. The results are shown in Fig. 3d. There is a relatively small parameter space for a fast reset on the order of 31 ns due to interaction between both qubit $|1\rangle$- and $|2\rangle$-state population with the coupler, with around 5% of the population remaining in the $|1\rangle$ state while the rest is in the $|0\rangle$ state. This is due to the proximity of the qubit Q_1 to Q_0 in frequency, limiting the furthest extent of the adiabatic pulse and thus the adiabadicity of the pulse. Therefore, we are able to reset both the $|1\rangle$ and the $|2\rangle$ states with the same pulse parameters, although the reset of the $|2\rangle$ state is only partially complete with a single pulse.

To improve the reset fidelity, we repeat the same reset scheme with another coupler. In practice, the implementation is realized with the coupler C_0 and C_2, both of which are coupled to Q_0. By preparing the $|1\rangle$ and $|2\rangle$ states separately, we observe that the $|1\rangle$-state reset can achieve an error below 1 %, while the reset error for the $|2\rangle$ state is close to 10% (see Suppl. Note III). From this, we can estimate that two successive reset operations with similar success probability can achieve a total fidelity of $1 - 0.1^2 = 99\%$, albeit at the cost of double the reset time.

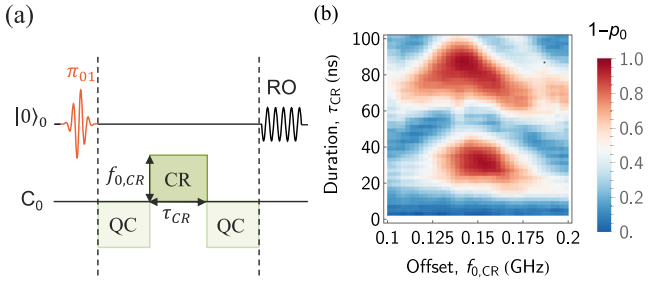

Fig. 4 | Coupler-resonator SWAP calibration. a Pulse scheme to characterize the coupler-resonator coupling strength and CR SWAP gate. **b** Rabi oscillations between the populations of the coupler and the resonator. The observed full swapping occurs at 54 ns, corresponding to a coupling strength of 18.5 MHz and a CR SWAP gate of 27 ns.

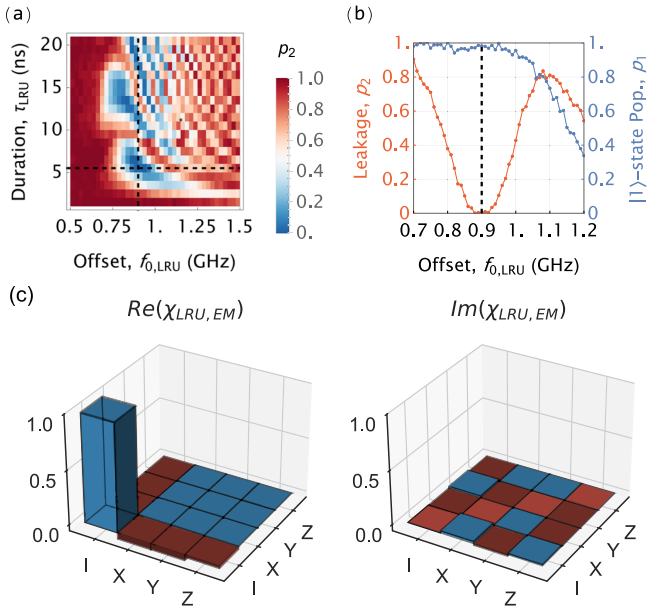

Fig. 5 | Calibration and verification of the LRU protocol. a Calibration of the square pulse used in the LRU, which is defined by two parameters: pulse duration τ_{LRU} and coupler offset $f_{0,LRU}$. Qubit Q_1 is initially prepared in the $|2\rangle$ state before the application of the pulse. The dashed lines indicate the parameters with minimal measured leakage. **b** Measured $|2\rangle$-state leakage (red) and the effect of the pulse on the $|1\rangle$-state (blue) population when Q_1 is prepared in the $|2\rangle$ (red) and $|1\rangle$ (blue) state, respectively. **c** Quantum process tomography (QPT) results for applying the LRU to Q_1, with the real and imaginary parts of the χ matrix shown separately, and blue (red) color represents positive (negative) values. The process fidelity is 99.20% when the LRU process is compared to an ideal identity gate. State-preparation-and-measurement (SPAM) errors in the QPT are mitigated, as explained in Suppl. Note IV.

Coupler-resonator SWAP gate

The next step of the reset protocol is to remove the excitation in the coupler by resonant interaction with the qubit readout resonator, as shown in Fig. 2d. Due to the direct capacitive coupling between the coupler and the qubit readout resonator and the indirect coupling mediated by the qubit, it is possible to implement this scheme without changing the architecture of the device.

To calibrate the coupler-resonator SWAP, which is a diabatic square pulse defined by two parameters, coupler offset f_{0,CR_d} and duration τ_{CR_d}, we start by measuring the coupling strength between the coupler and the resonator and implement the pulse sequence shown in Fig. 4a. We first prepare the qubit Q_0 in the $|1\rangle$ state and then apply the reset flux pulse, starting with a QC SWAP to populate the coupler. A diabatic square pulse is used during calibration to observe the oscillation of the excitation between the qubit Q_0 and the coupler C_0. Afterwards, we apply another diabatic square pulse of an opposite sign to observe the population oscillation between coupler C_0 and resonator R_1, which is lower in frequency than R_0. A Rabi oscillation between the coupler and the resonator population is observed and shown in Fig. 4b. The corresponding coupling rate is calculated to be 18.5 MHz, of which 1.4 MHz is contributed by the indirect coupling via the qubit, estimated from $g_{qr} \cdot g_{qc}/\Delta_{qr}$. The rest of the coupling strength is the direct capacitive coupling between the coupler and the resonator as a design feature of the flip-chip architecture. Similar strength is observed when coupling C_0 to the other resonator R_1, with a measured coupling strength of 16.1 MHz, with 1.9 MHz being indirect coupling. We then use a 27 ns square pulse (duration chosen in the center of the available parameter space to be robust against parameter drift) to perform the CR SWAP with a remaining population of 1.73% in the coupler, which can be further improved by using a resonator with a faster decay rate[36–38]. Note that the CR SWAP can be applied to all couplers simultaneously to reduce sequence time. To be able to reset multiple excitations in the coupler in a single process, an adiabatic transition can be used [8]. However, due to the relatively small coupling rate between the coupler and the resonator on our current device (compared to that between the qubit and its resonator, which is on the order of a hundred MHz), the adiabatic process is too slow compared to a diabatic transition, which should be considered as a factor in future iterations of chip design.

Leakage reduction unit with diabatic pulse

Qubit leakage outside of the computational space is a major source of errors. For example, a protocol to specifically target the $|2\rangle$ state of the qubit without disrupting the $|1\rangle$-state population is necessary for successful error correction. An LRU on the qubit Q_1 can be implemented by moving the coupler C_1 to where the $|1_1 1_c\rangle$ and $|2_1 0_c\rangle$ states of the Q_1-C_1 system are on resonance, as shown in Fig. 2c. The coupler C_1 that implements the LRU is parked below Q_1 to avoid disruption of its computational subspace.

We prepare Q_1 in the $(|1\rangle + |2\rangle)/\sqrt{2}$ superposition state, and apply the flux pulse to move the coupler C_1 such that the $|2_1 0_c\rangle$ state is on resonance with the $|1_1 1_c\rangle$ state. The LRU pulse shape is chosen to be a simple square pulse such that the interaction is fast and diabatic. This minimizes the effect on the qubit $|1\rangle$-state population. An extra π_{01} pulse is added after the LRU, since the readout fidelity is higher when measuring the $|0\rangle$-state population. The results in Fig. 5a show the measured leakage error $\epsilon_L = p_2$ as a function of the pulse parameter τ_{LRU} and $f_{0,LRU}$. It takes 5 ns to complete the population swapping from the $|2_1 0_c\rangle$ to the $|1_1 1_c\rangle$ state.

To verify the effect of the LRU on the computational subspace of Q_1, we first measured the effect on the population of Q_1 when this qubit is initially prepared in the $|1\rangle$ state, as shown in Fig. 5b. The $|1\rangle$-state population at the optimal LRU pulse parameters, as marked by the dashed line, is measured to be 99.33%. To complete the verification, we proceed to compare the LRU protocol with an identity (I) gate through quantum process tomography (QPT)[39,40]; since the LRU should ideally not disturb the computational subspace, it should act as an I gate. A virtual Z gate is calibrated to compensate for the phase shift on Q_1 caused by the LRU pulse, which is applied to the successive XY drive pulses after the LRU pulse with no physical time overhead during the QPT experiment. The fidelity of the measured χ matrix is calculated to be 99.20% when compared to the I gate, which is on par with other, slower state-of-the-art attempts at LRU implementation[11,25].

Furthermore, the LRU can be implemented simultaneously with the reset protocol on the other qubit, since it uses a different coupler, C_1. Similarly to the reset protocol, after interacting with the qubits, all couplers are made to adiabatically interact with the resonators simultaneously to transfer the couplers' population.

Single-shot verification

To fully characterize the reset and LRU performance, we prepare the two qubits in all nine combinations of two-qubit states in the first- and second-

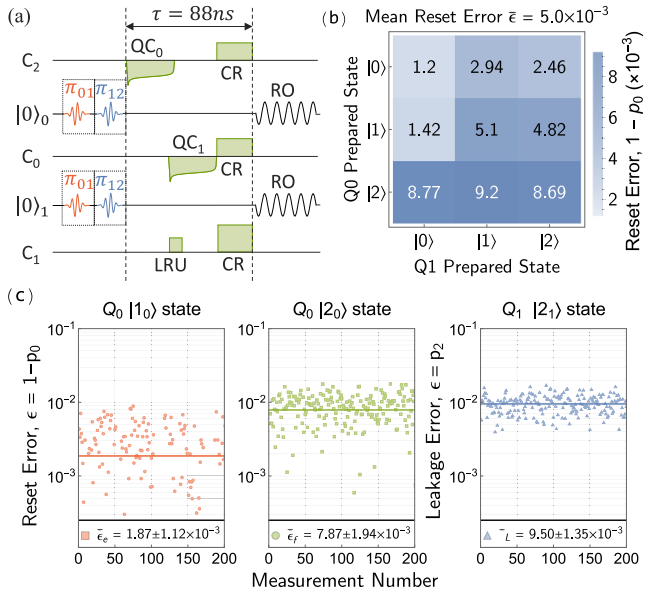

Fig. 6 | Pulse sequence and performance verification with single-shot readout. **a** The pulse sequences include the state preparation of two qubits, flux pulses applied on three couplers for reset and leakage reduction, and readout of the qubit population. The total duration of the flux pulse sequence is 88 ns. All nine combinations of two-qubit initial states in the first- and second-excitation subspaces are prepared and measured. **b** Single-shot readout results of Q_0 when all nine two-qubit states have been prepared, and the reset operation has been performed. The mean reset error for Q_0 is calculated from the average of all combinations. **c** Single-shot readout results for repeated applications of the protocol to three out of the nine combinations, where Q_0 is prepared in the $|1\rangle$ or $|2\rangle$ state or Q_1 is prepared in the $|2\rangle$ state, respectively. The measurement is repeated 200 times to test the stability of the protocol.

excitation subspaces, i.e., $|0_0 0_1\rangle$, $|0_0 1_1\rangle$, $|0_0 2_1\rangle$, etc. Then, we execute the full reset protocol, including $|1\rangle$- and $|2\rangle$-state QC SWAP, CR SWAP, and LRU with the two qubits (Q_0 and Q_1) and the three couplers (C_0, C_1, and C_2), as shown in Fig. 6a. With the measurement protocol established, we employ the covariance matrix adaptation evolution strategy (CMA-ES) algorithm to optimize the pulse parameters g, f_τ, and f_0 of each reset pulse to achieve a lower reset error[41].

Time-wise, resetting only the $|1\rangle$ state of the qubit Q_0 requires only 9 ns. However, to reset both the $|1\rangle$ and $|2\rangle$ states, we need to apply flux pulses on couplers C_0 and C_2 sequentially; these pulses are 31 ns and 30 ns long, respectively. The CR SWAP takes 27 ns while the leakage reduction unit needs a 5 ns-long pulse, which can start at the same time as the QC SWAP pulses. Therefore, the total time needed to implement both reset and LRU is 88 ns.

Each of the nine states is prepared and measured for 10,000 shots with single-shot readout (see Suppl. Note V), which set the lower limit on error to be 10^{-4} for each round of measurement. The results for each measurement are illustrated as a matrix in Fig. 6(b) as an example to show the reset error on Q_0. The first row of the matrix, where Q_0 is prepared in the $|0\rangle$ state, shows that the reset pulse does not bring any additional excitation to the qubit. The average of the second and the third rows, where Q_0 is prepared in the $|1\rangle$ and $|2\rangle$ states, respectively, represents the reset error for these states of Q_0. Simultaneously, the leakage population in Q_1 is measured for all these nine combinations, and we average over the third column, where Q_1 is prepared in the $|2\rangle$ state, to calculate the remaining leakage error. To understand the long-term stability and error margin, the results are gathered from 200 repeated measurements as illustrated in Fig. 6c. On average, the adiabatic reset protocol achieves a reset error of 1.87×10^{-3} (7.87×10^{-3}) for the $|1\rangle$ ($|2\rangle$) state. Meanwhile, the leakage reduction reaches an error of 9.50×10^{-3}. Over time, all three components are robust against random fluctuations during the span of at least a few hours.

DISCUSSION

In summary, we have implemented a fast, high-fidelity, and unconditional qubit reset protocol on fixed-frequency qubits coupled with a tunable coupler. Using adiabatic flux pulses on the couplers, our reset protocol achieves a reset error of $(1.87 \pm 1.12) \times 10^{-3}$ for the $|1\rangle$ state within 9 ns, and $(7.87 \pm 1.94) \times 10^{-3}$ for the $|2\rangle$ state in 61 ns. We also perform leakage reduction, on the qubit in 5 ns with a remaining leakage error of $(9.50 \pm 1.35) \times 10^{-3}$. Afterwards, the population in the coupler can be transferred to the readout resonator in 27 ns. In total, the combination of qubit reset, leakage reduction, and coupler reset takes only 88 ns to complete. The reset error we achieved is below the suggested threshold for quantum error correction to achieve improvement over no-reset schemes[42], which is between 10^{-2} and $10^{-2.5}$, together with the additional benefit of removing leakage in both qubits. The reset pulses are straightforward to tune up, with at most four parameters completely defining the entire pulse shape. Remarkably, the reset of one qubit and the leakage reduction of the other qubit can run simultaneously to achieve maximal efficiency due to the usage of all available coupler elements. Moreover, we have recently demonstrated[30] that our processor has a low level of crosstalk, which is promising for the further scale-up of our design.

The main limitation on the fidelity of the reset protocol is found to be the frequency separation of the qubit pair. With only 642 MHz of spacing between the two qubits, the adiabatic pulses have a limited frequency range to evolve back to the initial state of the coupler in the dispersive regime, which leads to an incomplete adiabatic transition. Another limiting factor is the small anharmonicity of the couplers on the current device. During a $|2\rangle$-state reset operation, the anharmonicities of coupler and qubits affect the detunings between the energy levels in the second-excitation subspace. These detunings impose a speed limit on the adiabatic process. The transition speed of the coupler energy levels needs to match ideally with the coupling rates between the respective levels according to the adiabatic condition to ensure a perfect population exchange. Further investigation on a generalized optimal pulse shape for adiabatic transition in the second-excitation subspace is needed to improve the fidelity even further, and depends on the anharmonicities. Likewise, during LRU operation, the small anharmonicity of the coupler leads to the undesired interaction with the $|1\rangle$ state of the qubits when their energy levels are close in frequency. Further design iterations and development in pulse-shaping techniques to alleviate these undesirable effects are currently under investigation with more theoretical simulations and better parameter-optimization algorithms.

Additionally, the slow decay of photons in the resonators, limited by resonator linewidths of 0.427 MHz and 0.294 MHz, prevented the verification of repeated reset with our protocol. These constraints can be mitigated by the addition of Purcell filters in the readout circuit, which enables effective resonator linewidths of more than 10 MHz without detrimental effects on qubit lifetimes[36–38], leading to a photon decay time on the order of a hundred nanoseconds. Furthermore, since the coupling between the resonator and coupler was initially undesirable during the design phase and therefore made small, adiabatic multi-level reset of the coupler, similar to previous demonstrations[8], would cost several hundreds of nanoseconds to implement on our current device, which can be part of future design considerations. Finally, we note that thermal populations in the couplers and resonators can set a lower bound for the reset protocol.

To see how to scale up the reset and LRU protocol in the surface-code implementation based on a 2D square grid, we can start by estimating the ratio between the number of qubits and couplers. For a code distance d, there will be d^2 data qubits, $d^2 - 1$ ancilla qubits, and $c_d = 4d(d-1)$ couplers. The reset and LRU protocol will need $c_r = 3 \cdot d^2 - 1$ couplers to fully implement the scheme. For $d > 3$, c_d is always greater than c_r, thus guaranteeing the implementation of our protocol without the need for additional elements.

For a general 2D square grid of qubits, placed alternatingly in higher- and lower-frequency groups[30,31], we can have each qubit connected to one coupler A that is placed higher in frequency than the higher-frequency qubits, two couplers B and D that are placed in between the two frequency groups, and one coupler C placed lower in frequency than the lower-

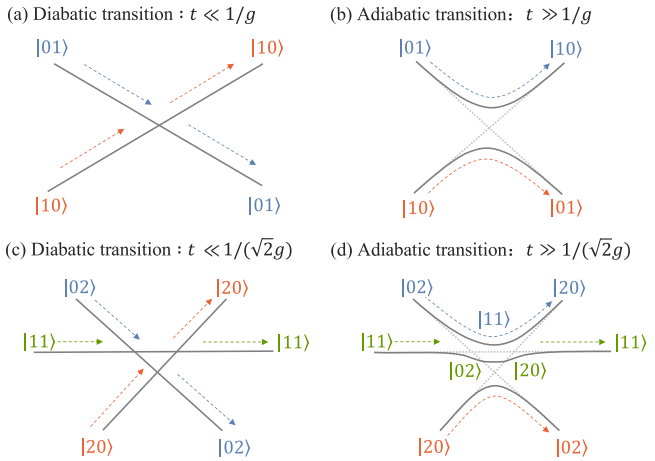

Fig. 7 | Diabatic and adiabatic transitions. The qubit and coupler energy levels ($|$ qubit, coupler $\rangle$) are coupled with strength g and $\sqrt{2}g$ for interactions within the (**a**, **b**) first- and (**c**, **d**) second-excitation subspace, respectively. The qubit level is stationary while the coupler is transiting across with a duration of time scale T. There are two limiting scenarios: (**a**, **c**) in a fast diabatic transition, $gT < 1$, the population stays on its original trajectory; (**b**, **d**) in a slow adiabatic transition, $gT \gg 1$, the population is swapped to the other energy level during the interaction.

frequency qubits. We can then, in a first time step, reset all higher-frequency qubits through coupler A while performing leakage reduction on all lower-frequency qubits through coupler C; in a second time step, we perform leakage reduction on all higher-frequency qubits through coupler B and reset all lower-frequency qubits through coupler D. However, other coupler placements may be more favorable from the perspective of what two-qubit gates one wants to perform.

In conclusion, we have demonstrated the capability to initialize the state of fixed-frequency qubits using tunable couplers, enabling faster measurement cycles and reduction of leakage population in quantum-computing applications.

Methods

System Hamiltonian

We consider the three-mode system in Fig. 1 consisting of a fixed-frequency transmon capacitively coupled to a readout resonator and a tunable transmon that acts as the coupler element. On the timescales of the reset operations, we assume that the resonator is the main lossy element and that the drives are sufficiently weak to invoke the rotating-wave approximation (RWA). Under these assumptions, we model the qubit and the coupler as Kerr oscillators[26] with anharmonicities α_q and α_c and the resonator as a lossy harmonic oscillator with relaxation rate κ. As such, we use the system Hamiltonian

$$\begin{aligned} H = &\sum_{i=q,c}\left(\omega_i a_i^\dagger a_i + \tfrac{\alpha_i}{2} a_i^\dagger a_i^\dagger a_i a_i\right) + \omega_r a_r^\dagger a_r \\ &+ \sum_{i=c,r} g_{iq}\left(a_i^\dagger a_q + a_q^\dagger a_i\right) + g_{cr}\left(a_c^\dagger a_r + a_r^\dagger a_c\right), \end{aligned} \tag{2}$$

where the subscripts q, c, and r label the qubit, coupler, and resonator, respectively, ω_i is the frequency of oscillator i, and g_{ij} is the coupling strength between oscillator i and j. The coupler frequency $\omega_c = \omega_c(\Phi(t))$ is tunable via the magnetic flux $\Phi(t)$ that threads through the SQUID loop of the coupler. Note that we include in this model a stray coupling g_{cr} between the coupler and the resonator. Since the coupler and resonator are not directly coupled (see Fig. 1), we assume that the stray coupling is smaller than the other coupling strengths, i.e., $|g_{cr}| \ll g_{qc}, g_{qr}$.

Note that $[H, N] = 0$, where $N = a_q^\dagger a_q + a_c^\dagger a_c + a_r^\dagger a_r$ is the total excitation number. Hence, the system Hamiltonian is excitation-number conserving, which is due to the fact that all terms in H contain an equal number of annihilation and creation operators. Importantly, this means that H decouples into different blocks labeled by N such that each block can be studied separately. The dynamics of a qubit starting in, e.g., its first excited state can hence be studied within the first-excitation subspace. We will use this assumption repeatedly below.

Adiabatic Landau–Zener–Stückelberg transitions

Underlying the reset protocol demonstrated in this article is the idea that we can adiabatically transfer excitations, i.e., implement SWAP gates, between the qubit, coupler, and resonator. In this section, we review the theory for adiabatic state transfers to explain how the coupler can be adiabatically tuned to transfer excitations from the qubit to the resonator. In particular, we focus on the case in Fig. 3c of transferring the first-qubit-excitation to the coupler: $|100\rangle \to |010\rangle$, where we use the Fock-state labeling $|q, c, r\rangle$.

For the qubit-coupler SWAP gate, the resonator is far detuned from the qubit ($\omega_r - \omega_q \gg g_{rq}$) such that we neglect its contribution to the dynamics. The dynamics of the first-excitation subspace reduces to an effective two-level system (TLS) formed by the qubit and the coupler near resonance:

$$H_{qc}^{\mathrm{TLS}} = \begin{bmatrix} \Delta_{qc}/2 & g_{qc} \\ g_{qc} & -\Delta_{qc}/2 \end{bmatrix}, \tag{3}$$

with detuning $\Delta_{qc} = \omega_q - \omega_c$. To understand the adiabatic state transfer in the reset protocol, where we initialize in $|100\rangle$ and transition to $|010\rangle$, we consider the dynamics as a Landau–Zener–Stückelberg (LZS) problem[43–45]. In the LZS problem, the detuning evolves linearly in time such that $\Delta_{qc} = -\nu_\Delta t$, where $\nu_\Delta = \partial_t \omega_c(t) > 0$ is the constant speed at which the coupler frequency increases, or is ramped up with.

As illustrated in Fig. 7, the time evolution in the LZS problem is separated into a diabatic or an adiabatic regime depending on the time scales of the ramp up. The adiabatic theorem[46] gives that the change in the detuning is adiabatic if the adiabatic condition is satisfied:

$$\frac{\left|\sum_{n\neq m}^{M} \frac{\langle\Psi_m(t)|\partial_t H|\Psi_n(t)\rangle}{E_m(t)-E_n(t)}\right|}{|E_m(t) - \mathrm{i}\langle\Psi_m(t)|\partial_t\Psi_m(t)\rangle|} \ll 1, \tag{4}$$

here stated for an M-level system with instantaneous eigenstates $|\Psi_m(t)\rangle$ and instantaneous eigenenergies $E_m(t)$, where $\partial_t\Psi_m(t)$ denotes the time derivative of the state. During adiabatic dynamics, a system initially in the eigenstate $|\Psi_m(0)\rangle$ evolves as the instantaneous eigenstate $|\Psi_m(t)\rangle$ (up to a time-dependent phase). For the two-level system, the minimum detuning between the eigenstates occurs at $t = 0$, $\Delta_{\min} = 2g_{qc}$. Using this in (4) sets the time scale $\nu_\Delta \sim 1/T$ for the diabatic and adiabatic regimes in Fig. 7. If the ramp-up speed is on a timescale of $T \gg 1/g_{gc}$, the evolution is said to be adiabatic. Otherwise, for $T < 1/g_{gc}$, the evolution is diabatic.

If we suppose that the initial qubit state $|\Psi(0)\rangle = |100\rangle$ is an initial eigenstate and evolves fully adiabatically, its time evolution then follows the instantaneous eigenstate $H_{qc}|\Psi_+(t)\rangle = E_+(t)|\Psi_+(t)\rangle$. The positive instantaneous eigenenergy is

$$E_+(t) = \sqrt{\left(\frac{\nu_\Delta t}{2}\right)^2 + g_{qc}^2}. \tag{5}$$

We note that for large t, i.e., detunings $\nu_\Delta t \gg g_{qc}$, the instantaneous eigenenergy matches the coupler frequency: $\lim_{t\to\infty} E_+(t) = \omega_c/2$. Hence, the initial state $|100\rangle$ has adiabatically evolved to the state $|010\rangle$. This is the process used in the reset protocol to transfer a single excitation in the qubit to the coupler.

Importantly, if the dynamics are not fully adiabatic, some excitation will remain in the qubit. The remaining population in the qubit after the

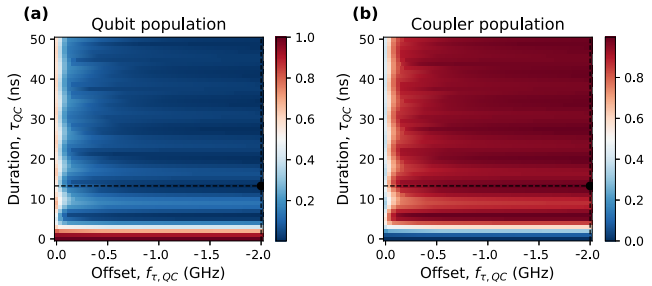

Fig. 8 | Simulated QC SWAP for initial state $|100\rangle$. a Time evolution of the qubit population, and (**b**) of the coupler population as a function of coupler frequency offset $f_{\tau,QC}$ and pulse duration τ_{QC}. The system is simulated using the designed pulse shape in (12), which implements a SWAP operation between the qubit and the coupler. The dashed line indicates the peak population in the coupler, corresponding to the maximum population transferred from the qubit. We define the reset error as the remaining population in the qubit after this transfer.

transition is given by the LZS transition probability

$$P_{\text{trans}} = \exp\left(-\frac{2\pi g_{qc}^2}{v_\Delta}\right). \tag{6}$$

Note that larger values of g_{qc} exponentially suppress the remaining population, which can be attributed to the increase in the energy gap at the avoided level crossing in Fig. 7.

Adiabatic transitions of second-excited states

Adiabatic transitions are also feasible between states with more than one excitation. We exploit this dynamical process in Fig. 3d to reset the second-excited state of the qubit. Here, we elucidate the transfer of two excitations from the qubit to the coupler in the form of the transition $|200\rangle \rightarrow |020\rangle$.

Similar to the single-excitation case, we suppose that the resonator is far detuned from the qubit ($\omega_r - \omega_q \gg g_{rq}$) to neglect its effect on the dynamics. The remaining states in the second-excitation subspace are $|200\rangle$, $|110\rangle$, and $|020\rangle$. We model their dynamics as an effective three-level system (3LS) using the Hamiltonian

$$H_{qc}^{3\text{LS}} = \begin{bmatrix} \Delta_{qc}+\alpha_q & \sqrt{2}g_{qc} & 0 \\ \sqrt{2}g_{qc} & 0 & \sqrt{2}g_{qc} \\ 0 & \sqrt{2}g_{qc} & -\Delta_{qc}+\alpha_c \end{bmatrix}, \tag{7}$$

which derives from (2). Assuming an initial state $|200\rangle$ at $t = -\infty$ and that the dynamics is adiabatic [recall (4)], the transfer to the state $|020\rangle$ is illustrated in Fig. 7c, d during a linear change of the detuning $\Delta_{qc} = -v_\Delta t$. The figure shows the case of $|\alpha_q + \alpha_c| \gg \sqrt{2}g_{qc}$. In this case, the transfer to $|020\rangle$ approximately occurs in two steps. First, the detuning evolves through the resonance $\Delta_{qc} = -\alpha_q$ and $|200\rangle$ transfers to the intermediate state $|110\rangle$. Second, the detuning passes the resonance $\Delta_{qc} = -\alpha_c$ and $|110\rangle$ transfers to $|020\rangle$. We note that the two steps of the transition overlap if $|\alpha_q + \alpha_c| \gg \sqrt{2}g_{qc}$ is not satisfied, but the end result is the same.

Adiabatic pulse shaping

In the two previous sections, the adiabatic transitions were described using a linear ramp up in the coupler frequency. Generally, the linear pulse is not ideal to achieve fast adiabatic transitions, which is why they are primarily not used for the reset pulses in Fig. 3. To speed up the adiabatic transitions, we use the Roland and Cerf protocol[32,33] to derive a pulse shape that is faster and still satisfies adiabaticity. We assume that the adiabatic condition in (1) is satisfied for every infinitesimal time interval from t to $t + dt$:

$$\sum_{n\neq m}^{M} \frac{|\langle \Psi_n(t)|\partial_t H(t)|\Psi_m(t)\rangle|}{|E_n(t) - E_m(t)|^2} \ll 1, \tag{8}$$

for all $n \neq m$. Note that (8) is a more restrictive adiabatic condition than (4), and the former condition can be derived from the later one by assuming for all $n \neq m$:

$$|E_m(t) - i\langle \Psi_m(t)|\partial_t \Psi_m(t)\rangle| > |E_m(t) - E_n(t)|. \tag{9}$$

For the two-level system modeling the qubit-coupler single-excitation SWAP in (3), the adiabatic condition in (8) simplifies to

$$\left|\frac{\partial \Delta_{qc}(t)}{\partial t}\right| \ll \frac{(\Delta_{qc}^2(t) + 4g_{qc}^2)^{\frac{3}{2}}}{g_{qc}}. \tag{10}$$

We multiply the right-hand side of (10) with a scaling prefactor β to obtain a differential equation for the qubit-coupler detuning $\Delta_{qc}(t)$:

$$\left|\frac{\partial \Delta_{qc}(t)}{\partial t}\right| = \beta \frac{(\Delta_{qc}^2(t) + 4g_{qc}^2)^{\frac{3}{2}}}{g_{qc}}. \tag{11}$$

Note that (10) is satisfied for $\beta \ll 1$.

Given the temporal boundary conditions $\Delta_{qc}(0) = f_0$ and $\Delta_{qc}(\tau) = f_\tau$ for a pulse duration of τ, we solve (11) to find the pulse shape

$$\Delta_{qc}(t) = -\frac{8g_{qc}(\beta g_{qc} t + \delta)}{\sqrt{1 - 16(\beta g_{qc} t)^2 - 32\beta\delta g_{qc} t - 16\delta^2}}, \tag{12}$$

where the boundary conditions give

$$\beta = \frac{-4\delta\left(f_\tau^2 + 4g_{qc}^2\right) - f_\tau\sqrt{f_\tau^2 + 4g_{qc}^2}\,\Big)}{4g_{qc}\tau(f_\tau^2 + 4g_{qc}^2)}, \tag{13}$$

$$\delta = -\frac{f_0}{4\sqrt{f_0^2 + 4g_{qc}^2}}. \tag{14}$$

Pulse shapes similar to (12), based on the Roland and Cerf protocol, can also be found in refs. 32,35,47–49.

Simulation of adiabatic transitions

We simulate the time evolution of the qubit-coupler-resonator system to evaluate the reset errors of qubit Q_0 as a function of the coupler frequency offset $f_{\tau,QC}$ and the pulse duration τ_{QC}. In particular, we use the Hamiltonian in (2) together with the detuning defined in (12), and the pulse shape shown in Fig. 3a to numerically integrate the Schrödinger equation with QuTiP [50,51] in the first- and second-excitation subspaces. The result for the first-excitation subspace is shown in Fig. 8. The color in Fig. 8a represents the population remaining in the qubit after a SWAP-like pulse, with red (blue) indicating high (low) residual population. The dashed lines mark the optimal parameter values that minimize the reset error, corresponding to maximum population transfer to the coupler. Conversely, Fig. 8b shows the coupler population under the same conditions, which is approximately one minus the qubit population, confirming the effectiveness of the transfer.

We note that in the experimental counterpart [see Fig. 3c], we observe deviations from the simulated ideal reset behavior, particularly visible as asymmetries and reduced contrast in the qubit population transfer. These distortions are likely due to low-frequency flux noise and

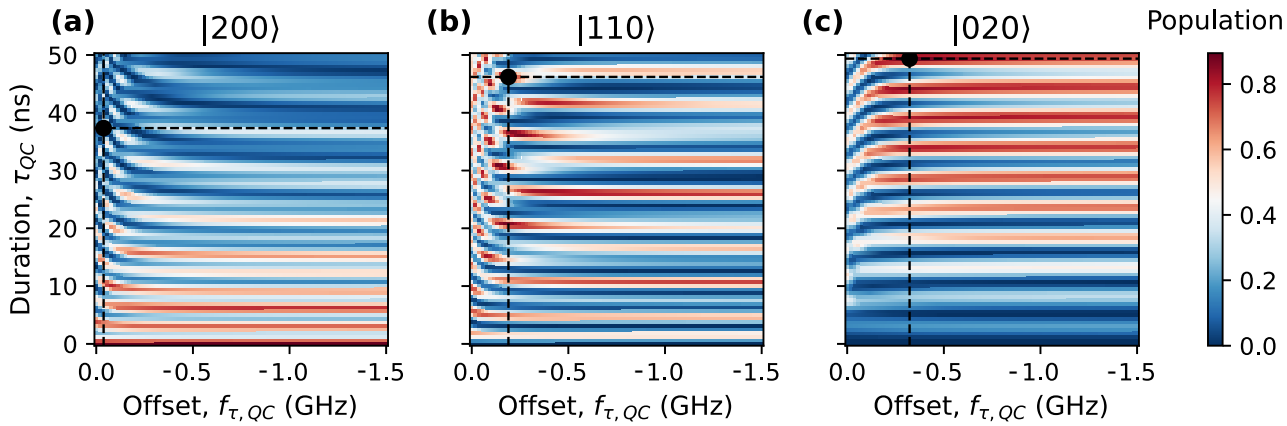

Fig. 9 | Simulated population dynamics in the two-excitation subspace. a Initial state population in |200⟩ and its transfer to (**b**)|110⟩ and (**c**)|020⟩, shown as a function of coupler frequency offset $f_{\tau,QC}$ and pulse duration τ_{QC}. The dashed lines mark the optimal parameter values based on the extremum (minimum or maximum) of each population. The color scale indicates population, with blue indicating low and red indicating high.

pulse distortions, which are not included in the simulation. Such noise can alter the effective detuning and coupling strength during the reset pulse, leading to reduced fidelity and variability in the optimal offset/duration parameters.

In Fig. 9, we show the simulation of the second-excitation subspace. The system is initialized in the two-excitation state |200⟩, where both excitations are in the qubit. Ideally, the applied pulse redistributes these excitations through the coupler into states such as |110⟩ and |020⟩, conserving the total number of excitations. This process is similar to a second-order SWAP operation. The results show that the population initially in |200⟩ is partially transferred to |110⟩ and |020⟩, depending on the pulse parameters. However, the minimum of the |200⟩ population in panel Fig. 9a does not align exactly with the maxima in panels Fig. 9b, c. This indicates that the population transfer is not fully directed to a single final state, and may instead be distributed between multiple output states.

The pulse used was optimized for dynamics in the first-excitation subspace. While this works well for standard SWAP operations, it may not perform optimally when multiple excitations are present. Including the two-excitation subspace in the pulse optimization could improve transfer fidelity and better control multi-excitation dynamics.

Data availability

All relevant data and figures supporting the main conclusions of the document are available on Zenodo (https://zenodo.org/records/16979513). Please refer to Giovanna Tancredi at tancredi@chalmers.se if needed. All relevant experimental code supporting the document is available online via GitHub (https://github.com/tergite/tergite-autocalibration). Please refer to Giovanna Tancredi at tancredi@chalmers.se if needed.

Code availability

All relevant experimental code supporting the document is available online via GitHub. Please refer to Giovanna Tancredi at tancredi@chalmers.se if needed.

Received: 18 November 2025; Accepted: 5 August 2026;
Published online: 15 August 2026

References

1. DiVincenzo, D. P. The Physical Implementation of Quantum Computation. *Fortschr. der Phys.* **48**, 771–783 (2000).
2. Wang, C. et al. Towards practical quantum computers: transmon qubit with a lifetime approaching 0.5 milliseconds. *npj Quantum Inf.* **8**, 3 (2022).
3. Biznárová, J. et al. Mitigation of interfacial dielectric loss in aluminum-on-silicon superconducting qubits. *npj Quantum Inf.* **10**, 78 (2024).
4. Bland, M. P. et al. 2D transmons with lifetimes and coherence times exceeding 1 millisecond, arXiv:2503.14798 (2025).
5. Egger, D. et al. Pulsed reset protocol for fixed-frequency superconducting qubits. *Phys. Rev. Appl.* **10**, 044030 (2018).
6. Geerlings, K. et al. Demonstrating a driven reset protocol for a superconducting qubit. *Phys. Rev. Lett.* **110**, 120501 (2013).
7. Moreira, M. S. et al. Realization of a quantum neural network using repeat-until-success circuits in a superconducting quantum processor. *npj Quantum Inf.* **9**, 118 (2023).
8. McEwen, M. et al. Removing leakage-induced correlated errors in superconducting quantum error correction. *Nat. Commun.* **12**, 1761 (2021).
9. Zhou, Y. et al. Rapid and unconditional parametric reset protocol for tunable superconducting qubits. *Nat. Commun.* **12**, 5924 (2021).
10. Magnard, P. et al. Fast and unconditional all-microwave reset of a superconducting qubit. *Phys. Rev. Lett.* **121**, 060502 (2018).
11. Yang, X. et al. Coupler-assisted leakage reduction for scalable quantum error correction with superconducting qubits. *Phys. Rev. Lett.* **133**, 170601 (2024).
12. Huber, G. B. P. et al. Parametric multi-element coupling architecture for coherent and dissipative control of superconducting qubits 2403.02203 (2024).
13. Lo, H.-K., Spiller, T. & Popescu, S. Introduction to quantum computation and informationhttps://www.worldscientific.com/doi/abs/10.1142/3724 (World Scientific, 1998).
14. Fowler, A. G., Mariantoni, M., Martinis, J. M. & Cleland, A. N. Surface codes: Towards practical large-scale quantum computation. *Phys. Rev. A* **86**, 032324 (2012).
15. Martinis, J. M. Qubit metrology for building a fault-tolerant quantum computer. *npj Quantum Inf.* **1**, 15005 (2015).
16. Chen, Z. et al. Exponential suppression of bit or phase errors with cyclic error correction. *Nature* **595**, 383–387 (2021).
17. Krinner, S. et al. Realizing repeated quantum error correction in a distance-three surface code. *Nature* **605**, 669–674 (2022).
18. Zhao, Y. et al. Realization of an error-correcting surface code with superconducting qubits. *Phys. Rev. Lett.* **129**, 030501 (2022).
19. Acharya, R. et al. Suppressing quantum errors by scaling a surface code logical qubit. *Nature* **614**, 676–681 (2023).
20. Acharya, R. et al. Quantum error correction below the surface code threshold. *Nature* **638**, 920 (2025).

21. Marques, J. F. et al. All-microwave leakage reduction units for quantum error correction with superconducting transmon qubits. *Phys. Rev. Lett.* **130**, 250602 (2023).
22. Miao, K. C. et al. Overcoming leakage in quantum error correction. *Nat. Phys.* **19**, 1780–1786 (2023).
23. Battistel, F., Varbanov, B. & Terhal, B. Hardware-efficient leakage-reduction scheme for quantum error correction with superconducting transmon qubits. *PRX Quantum* **2**, 030314 (2021).
24. Diniz, C. M., Bôas, C. J. V. & Santos, A. C. Scalable quantum eraser for superconducting integrated circuits 2409.16893 (2024).
25. Lacroix, N. et al. Fast flux-activated leakage reduction for superconducting quantum circuits. *Phys. Rev. Lett.* **134**, 120601 (2025).
26. Koch, J. et al. Charge-insensitive qubit design derived from the Cooper pair box. *Phys. Rev. A* **76**, 042319 (2007).
27. McKay, D. C. et al. Universal gate for fixed-frequency qubits via a tunable bus. *Phys. Rev. Appl.* **6**, 064007 (2016).
28. Yan, F. et al. Tunable coupling scheme for implementing high-fidelity two-qubit gates. *Phys. Rev. Appl.* **10**, 054062 (2018).
29. Kosen, S. et al. Building blocks of a flip-chip integrated superconducting quantum processor. *Quantum Sci. Technol.* **7**, 035018 (2022).
30. Kosen, S. et al. Signal crosstalk in a flip-chip quantum processor. *PRX Quantum* **5**, 030350 (2024).
31. Osman, A. et al. Mitigation of frequency collisions in superconducting quantum processors. *Phys. Rev. Res.* **5**, 043001 (2023).
32. Roland, J. & Cerf, N. J. Quantum search by local adiabatic evolution. *Phys. Rev. A* **65**, 042308 (2002).
33. Albash, T. & Lidar, D. A. Adiabatic quantum computation. *Rev. Mod. Phys.* **90**, 015002 (2018).
34. Stefanatos, D. & Paspalakis, E. Speeding up adiabatic passage with an optimal modified Roland-Cerf protocol. *J. Phys. A: Math. Theor.* **53**, 115304 (2020).
35. Malossi, N. et al. Quantum driving protocols for a two-level system: From generalized Landau-Zener sweeps to transitionless control. *Phys. Rev. A* **87**, 012116 (2013).
36. Jeffrey, E. et al. Fast Accurate State Measurement with Superconducting Qubits. *Phys. Rev. Lett.* **112**, 190504 (2014).
37. Walter, T. et al. Rapid High-Fidelity Single-Shot Dispersive Readout of Superconducting Qubits. *Phys. Rev. Appl.* **7**, 054020 (2017).
38. Chen, L. et al. Transmon qubit readout fidelity at the threshold for quantum error correction without a quantum-limited amplifier. *npj Quantum Inf.* **9**, 26 (2023).
39. D'Ariano, G. M. & Lo Presti, P. Quantum tomography for measuring experimentally the matrix elements of an arbitrary quantum operation. *Phys. Rev. Lett.* **86**, 4195–4198 (2001).
40. Huang, T. et al. Quantum process tomography with digital twins of error matrices 2505.07725 (2025).
41. Auger, A. & Hansen, N. A restart CMA Evolution Strategy with increasing population size. *2005 IEEE Congr. Evolut. Comput.* **2**, 1769–1776 (2005).
42. Gehér, G. P., Jastrzebski, M., Campbell, E. T. & Crawford, O. To reset, or not to reset – that is the question 2408.00758 (2024).
43. Stückelberg, E. Theory of Inelastic Collisions between Atoms. *Helvetica Physica Acta*369-423 (1932).
44. Landau, L. On the theory of transfer of energy at collisions I. *Physikalische Z. der Sowjetunion* **1**, 88 (1932).
45. Ivakhnenko, O. V., Shevchenko, S. N. & Nori, F. Nonadiabatic Landau-Zener-Stückelberg-Majorana transitions, dynamics, and interference. *Phys. Rep.* **995**, 1–89 (2023).
46. Sakurai, J. J. & Napolitano, J.Modern Quantum Mechanicshttps://www.cambridge.org/highereducation/books/modern-quantum-mechanics/DF43277E8AEDF83CC12EA62887C277DC (Cambridge University Press, 2020).
47. Bason, M. G. et al. High-fidelity quantum driving. *Nat. Phys.* **8**, 147–152 (2012).
48. Stefanatos, D. & Paspalakis, E. Resonant shortcuts for adiabatic rapid passage with only *z*-field control. *Phys. Rev. A* **100**, 012111 (2019).
49. Petiziol, F. et al. Accelerating adiabatic protocols for entangling two qubits in circuit QED. *Phys. Rev. A* **99**, 042315 (2019).
50. Johansson, J., Nation, P. & Nori, F. Qutip: an open-source Python framework for the dynamics of open quantum systems. *Computer Phys. Commun.* **183**, 1760–1772 (2012).
51. Lambert, N. et al. Qutip 5: the quantum toolbox in Python. *Phys. Rep.* **1153**, 1–62 (2026).

Acknowledgements

We would like to thank Per Delsing, Christopher W. Warren, Christian J. Križan, Anuj Aggarwal, Janka Biznárová, Guangze Chen, Huizhong Cao, and Jorge Fernandez-Pendas for valuable discussions and insights. The fabrication of our quantum processor was performed in part at Myfab Chalmers and flip-chip integration was done at VTT. The device simulations were enabled by resources provided by the Swedish National Infrastructure for Computing (SNIC) at National Supercomputer Centre (NSC) partially funded by the Swedish Research Council through grant agreement no. 2018-05973. This research was financially supported by the Knut and Alice Wallenberg Foundation through the Wallenberg Center for Quantum Technology (WACQT), the Swedish Research Council, and by the EU Flagship on Quantum Technology HORIZON-CL4-2022-QUANTUM-01-SGA project 101113946 OpenSuperQPlus100. A.F.K. also acknowledges support from the Swedish Foundation for Strategic Research (grant numbers FFL21-0279 and FUS21-0063).

Author contributions

L.C. performed the measurements and analysis of the results; S.K., H.L., D.S., R.R., and A.O. designed and simulated the device; L.C., B.L., and S.P.F. produced and developed the idea. S.P.F., Z.Y., A.Al., and T.A. carried out theoretical simulations of the system. L.C. and T.H. performed the process tomography. L.C., E.M., T.L., S.H., A.Am., M.D. and M.F.G. contributed to the implementation of the control methods. S.K., M.R., A.O., A.F.R., A.N., M.C., L.G., and J.G. participated in the fabrication of the device. L.C., S.P.F., T.A., Z.Y., T.H. wrote, and G.T., A.F.K., and J.By. edited the manuscript. A.F.K., J.By., and G.T. provided supervision and guidance during the project. All authors contributed to the discussions and interpretations of the results.

Funding

Open access funding provided by Chalmers University of Technology.

Competing interests

The authors declare no competing interests.

Additional information

Supplementary information The online version contains supplementary material available at https://doi.org/10.1038/s41534-026-01356-2.

Correspondence and requests for materials should be addressed to Liangyu Chen, Jonas Bylander or Giovanna Tancredi.

Reprints and permissions information is available at http://www.nature.com/reprints

Publisher's note Springer Nature remains neutral with regard to jurisdictional claims in published maps and institutional affiliations.

Open Access This article is licensed under a Creative Commons Attribution 4.0 International License, which permits use, sharing, adaptation, distribution and reproduction in any medium or format, as long as you give appropriate credit to the original author(s) and the source, provide a link to the Creative Commons licence, and indicate if changes were made. The images or other third party material in this article are included in the article's Creative Commons licence, unless indicated otherwise in a credit line to the material. If material is not included in the article's Creative Commons licence and your intended use is not permitted by statutory regulation or exceeds the permitted use, you will need to obtain permission directly from the copyright holder. To view a copy of this licence, visit http://creativecommons.org/licenses/by/4.0/.

© The Author(s) 2026